Electronic Supplementary Material (ESI) for Materials Horizons.

Supporting Information

Palliating Jahn-Teller distortion and locking lattice water with doped Fe (III) in birnessite toward fast and stable zinc-ion batteries

Xiang Li,‡[a] Yanchun Sun,‡[a] Le Zhou,[a] Haiyan Wang,*[a] Binbin Xie,*[b] Wen Lu,[a] Jiqiang Ning,[c] and Yong Hu*[d]

Experimental Section

Chemicals and raw materials: All the chemicals of analytical grade were purchased from Sinopharm Chemical Reagent Co., Ltd. (China) and used directly without further purification. The carbon paper (TGP-H-060) was obtained from Toray Co., Ltd. (Japan). The commercial zinc foil with a thickness of 100 μm was purchased from Sinopharm Chemical Reagent Co., Ltd. (China).

Synthesis of Fe-NMO·xH₂O: Fe doped $Na_{0.55}Mn_2O_4 \cdot xH_2O$ (Fe-NMO·xH_2O) was prepared using a coprecipitation method at room temperature. In a typical synthesis, 0.5 mmol of trisodium citrate dihydrate ($Na_3C_6H_5O_7 \cdot 2H_2O$), 3 mmol of NaOH, and 0.1 mmol of $(CH_3COO)_2Mn \cdot 4H_2O$ were dissolved in 40 mL of deionized water to get a clear solution A. 0.2 mmol of $K_3[Fe(CN)_6]$ was dissolved in 20 mL of deionized water to gain a clear solution B. Then, solution B was dripped into solution A under vigorous stirring for 1 min, and the mixture was aged for 24 h to obtain the precipitate. Finally, the resulting precipitate was collected, washed with deionized water and ethanol several times, and dried in an oven at 60 °C overnight to obtain Fe-NMO·xH_2O. The comparison samples of $Fe_{0.1}$-NMO·xH_2O, and $Fe_{0.3}$-NMO·xH_2O were synthesized by changing the amounts of $K_3[Fe(CN)_6]$ from 0.1 mmol to 0.3 mmol, respectively.

Synthesis of NMO·xH_2O: NMO·xH_2O was prepared using the similar method as Fe-NMO·xH_2O but without the addition of $K_3[Fe(CN)_6]$.

Synthesis of Fe-NMO·xH_2O-T: Fe-NMO·xH_2O was calcined at 300 °C for 1 h in air to prepare Fe-NMO·xH_2O-T.

Characterizations: The field-emission scanning electron microscopy (FESEM) images of the samples were operated on a scanning electron micro-analyzer (Hitachi S-4800). The microstructures of the materials were investigated with transmission electron microscopy (TEM) and high-resolution TEM (HRTEM), which were performed on a JEM-2100F field emission micro-analyzer at an accelerating voltage of 200 kV. Powder X-ray diffraction

(XRD) was carried out on a Bruker D8 Advance diffractometer with Cu-Kα radiation. Thermogravimetry analysis (TGA) was conducted on the NETZSCH STA449 F5 with a nitrogen flow. X-ray photoelectron spectroscopy (XPS) was carried out on an ESCALab MKII X-ray photoelectron spectrometer with Al Ka X-ray radiation as the excitation source. Raman spectra were collected on a Renishaw in Via-Refles with a 532 nm laser.

Assembly of Zn-ion batteries: The electrochemical performance of the materials was investigated by assembling a CR2025 coin cell. For the preparation of the cathode, Fe-NMO·xH_2O, polyvinylidene fluoride, and conductive carbon black with a mass ratio of 8:1:1 were dispersed in 1-methyl-2-pyrrolidone solvent and ground into a pulp. Then the pulp was coated on carbon paper with a mass loading of ~1.2 mg for the active materials and then dried in a vacuum oven at 80 °C for 12 h. Before assembly, the commercial zinc foil (100 μm) was polished with sandpaper, and wiped with ethanol to remove the surface oxide layer and impurities. The as-fabricated cathode and the processed Zn foil anode separated by a Whatman filter separator were further assembled into a CR2025 coin cell with 2 M $ZnSO_4$ and 0.2 M $MnSO_4$ aqueous solution (100 μL) as the electrolyte. In addition, to explore the energy storage mechanism of Fe-NMO·xH_2O, 0.2 M $MnSO_4$, 0.2 M $Zn(OTf)_2$ in acetonitrile (denoted as AN), and 0.2 M $Zn(OTf)_2$ in AN + 1 wt.% H_2O electrolytes with the same volume of 100 μL was also employed to assemble the Zn-ion battery.

Electrochemical measurements: The electrochemical performances were evaluated by cyclic voltammetry (CV), galvanostatic charge/discharge (GCD), and electrochemical impedance spectroscopy (EIS) measurements. CV and EIS data were collected on a CHI660E workstation. GCD was carried out on a LAND CT3001A battery testing system.

Computational details: All density functional theory (DFT) calculations[1,2] were carried out using the Projector-Augmented Wave (PAW) method[3] as implemented in the Vienna Ab-initio Simulation Package (VASP).[4] The exchange-correlation energy was described by the Perdew-Burke-Ernzerh (PBE) functional[5] developed by Perdew, Burke, and Ernzerhof at the generalized gradient approximation (GGA). The Hubbard-U corrections[6] (a U-J value of 4.0 for Mn and Fe) and DFT-D3 corrections[7] were taken into account for more accurate calculations. The kinetic energy cutoff of electron wave functions was set to 400 eV. The conjugated gradient method was performed to obtain all equilibrium geometries with the convergence threshold of energy and force to be 10^{-4} eV and 0.04 eV/Å, respectively. A five-layer model (an 11.82 Å × 11.40 Å × 16.19 Å box) was constructed for the bare $Na_{0.55}Mn_2O_4 \cdot xH_2O$ material (denoted as $NMO \cdot xH_2O$), which includes three MnO_2 (001) layers and two lattice water layers. Similarly, for Fe-doped material, a Mn atom on the topmost layer of $NMO \cdot xH_2O$ was substituted by a Fe atom, referred to as Fe-$NMO \cdot xH_2O$. In addition, we also built a Fe-doped model without lattice water for comparison (Fe-NMO), which had the cell size of 10.36 Å × 11.650 Å × 13.18 Å.

All calculations including geometry optimization, single-point energy, electronic density, and density of states were carried out under a periodic boundary condition using a gamma centered k-point mesh. A very large vacuum space of 40 Å in the z direction was adopted to eliminate interactions between successive slabs, especially for the calculations of the exfoliation energy (E_{exf}). The charge differential density and density of states were calculated and depicted with VASPKIT and VESTA.[8,9] The exfoliation energy was defined as:

$$\mathrm{E}_{exf} = \mathrm{E}_{layered} - \mathrm{E}_{enlarged\ 20\,\text{Å}} \tag{S1}$$

where $E_{layered}$, and $E_{enlayered\ 20\ \text{Å}}$ were the DFT calculated energies of the $NMO \cdot xH_2O$ or Fe-$NMO \cdot xH_2O$ material with normal interlayer spacing and enlarged interlayer spacing (20 Å). Similarly, the absorption energy (E_{abs}) between the materials ($NMO \cdot xH_2O$ or Fe-$NMO \cdot xH_2O$) and other species (the Zn atom or the water layer) was written as:

$$\mathrm{E}_{abs} = \mathrm{E}_{material+other} - \mathrm{E}_{other} - \mathrm{E}_{material} \tag{S2}$$

where $E_{material+other}$ was the total energy of material and other species, $E_{material}$ was the energy of the material and E_{other} was the energy of other species.

Calculations: The specific capacity (C_s, mAh g^{-1}) of the samples was calculated based on the discharge curve. The equation for calculating C_s is shown as follows:

$$C_{\mathrm{s}} = \frac{\int_0^t I\mathrm{d}t}{m} \tag{S3}$$

where I (mA) represents the discharge current, t (h) is the discharge time, and m (g) means the mass loading of the active materials.

Energy density E (Wh kg^{-1}) and power density P (W kg^{-1}) were calculated according to Equations S4 and S5, respectively:

$$E=C_{\mathrm{s}}V \tag{S4}$$

$$P = \frac{3600E}{t} \tag{S5}$$

where V (V) represents the platform voltage, t (s) is the discharge time.

The activation energy (E_a) is calculated according to the Arrhenius equation:

$$\frac{1}{R_{\mathrm{ct}}} = A\exp\left(-\frac{E_{\mathrm{a}}}{RT}\right) \tag{S6}$$

where R_{ct} represents the charge transfer resistance, A is pre-exponential factor, T and R are the temperature and the gas constant, respectively.

Supplementary Figures

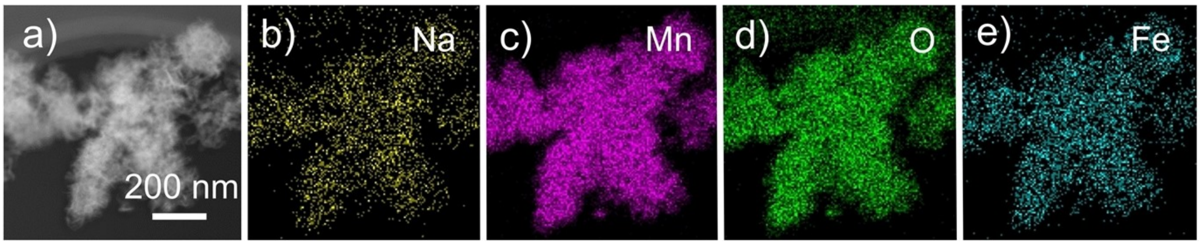

Fig. S1 (a) STEM image of the as-prepared Fe-NMO·xH_2O and corresponding elemental mapping images of (b) Na, (c) Mn, (d) O, (e) Fe.

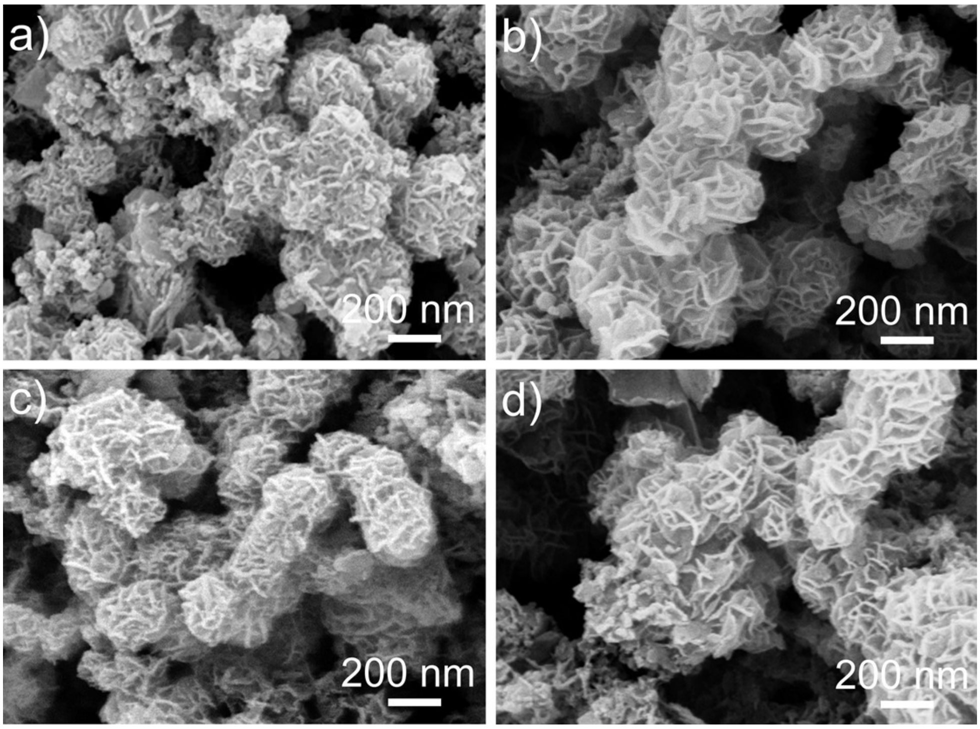

Fig. S2 FESEM images of the as-prepared (a) NMO·xH_2O, (b) $Fe_{0.1}$-NMO·xH_2O, (c) $Fe_{0.3}$-NMO·xH_2O, and (d) Fe-NMO·xH_2O-T samples.

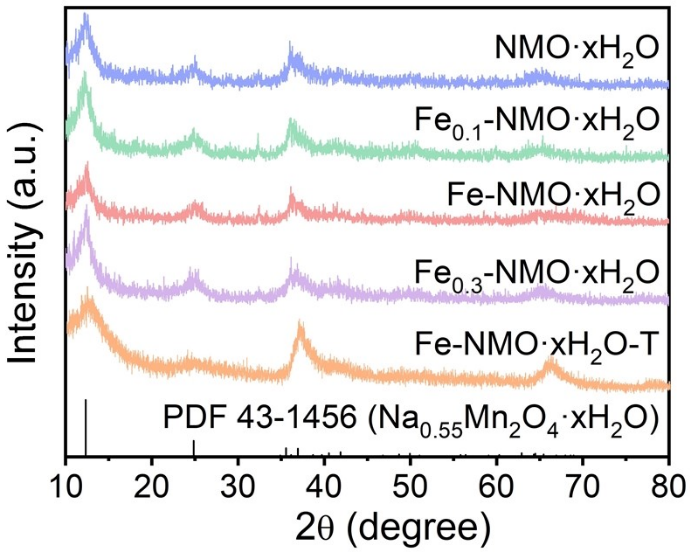

Fig. S3 XRD patterns of the as-prepared NMO·xH_2O, $Fe_{0.1}$-NMO·xH_2O, Fe-NMO·xH_2O, $Fe_{0.3}$-NMO·xH_2O and Fe-NMO·xH_2O-T samples.

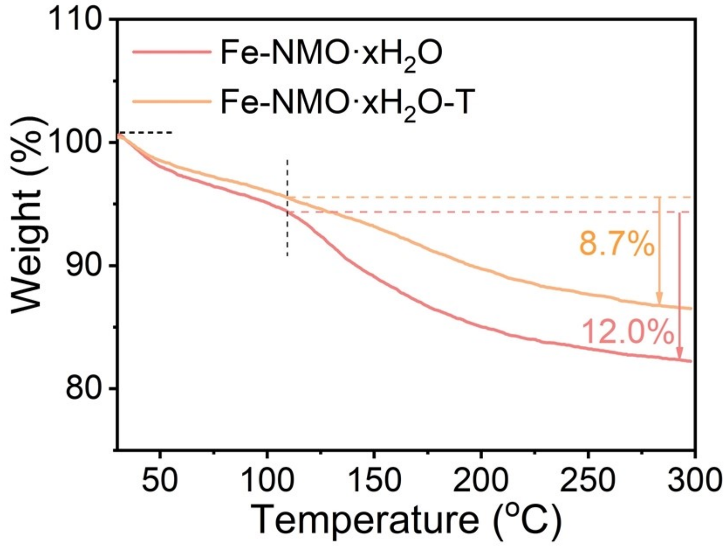

Fig. S4 TGA curves of the as-prepared Fe-NMO·xH_2O and Fe-NMO·xH_2O-T samples.

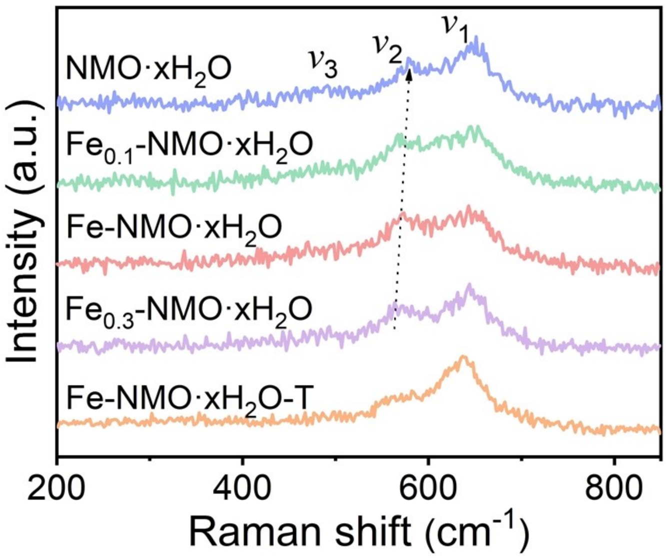

Fig. S5 Raman spectra of the as-prepared NMO·xH_2O, $Fe_{0.1}$-NMO·xH_2O, Fe-NMO·xH_2O, $Fe_{0.3}$-NMO·xH_2O and Fe-NMO·xH_2O-T samples.

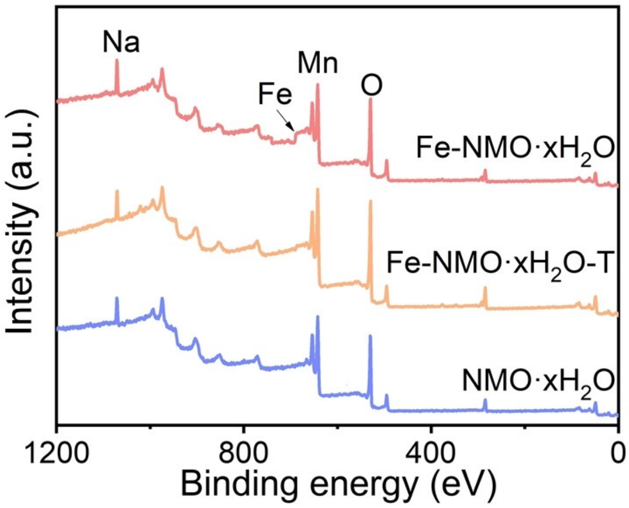

Fig. S6 XPS survey spectra of the as-prepared Fe-NMO·xH_2O, Fe-NMO·xH_2O-T, and NMO·xH_2O samples.

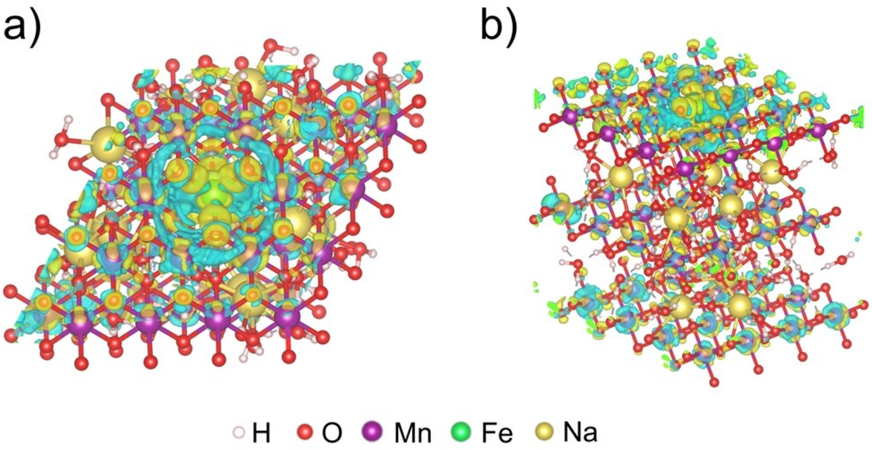

Fig. S7 Charge density difference distributions of Fe-NMO·xH_2O: (a) Top view, (b) Side view (blue and yellow represent electron-deficient and electron-rich regions, respectively).

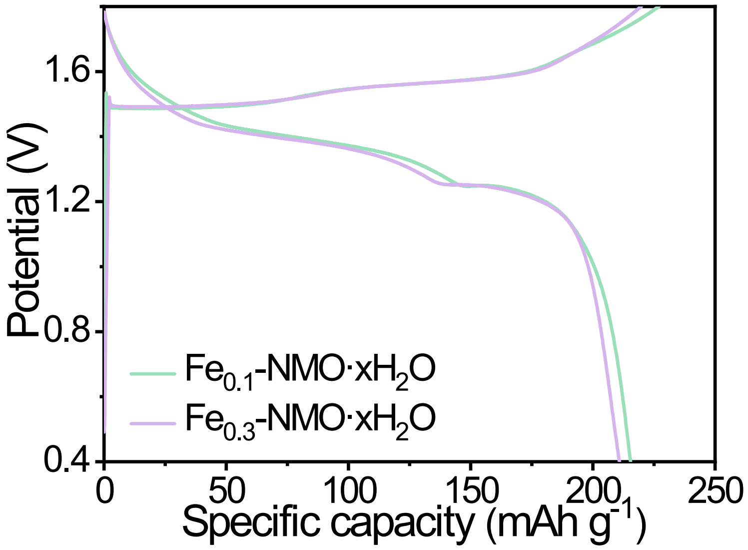

Fig. S8 GCD profiles of the $Fe_{0.1}$-NMO·xH_2O and $Fe_{0.3}$-NMO·xH_2O at 0.2 A g^{-1}.

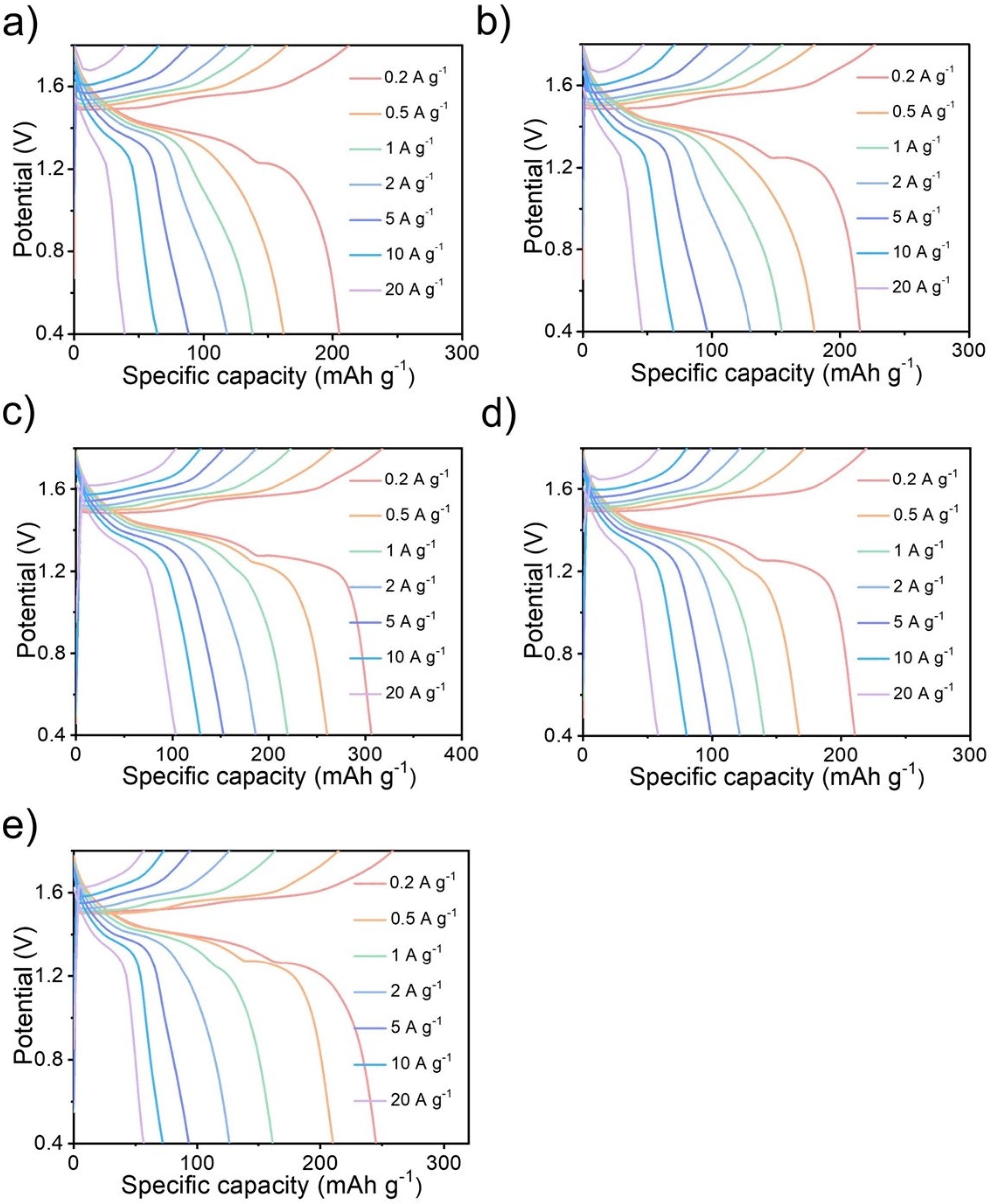

Fig. S9 GCD profiles of the (a) NMO·xH_2O, (b) $Fe_{0.1}$-NMO·xH_2O, (c) Fe-NMO·xH_2O, (d) $Fe_{0.3}$-NMO·xH_2O and (e) Fe-NMO·xH_2O-T at various current densities from 0.2 to 20 A g^{-1}.

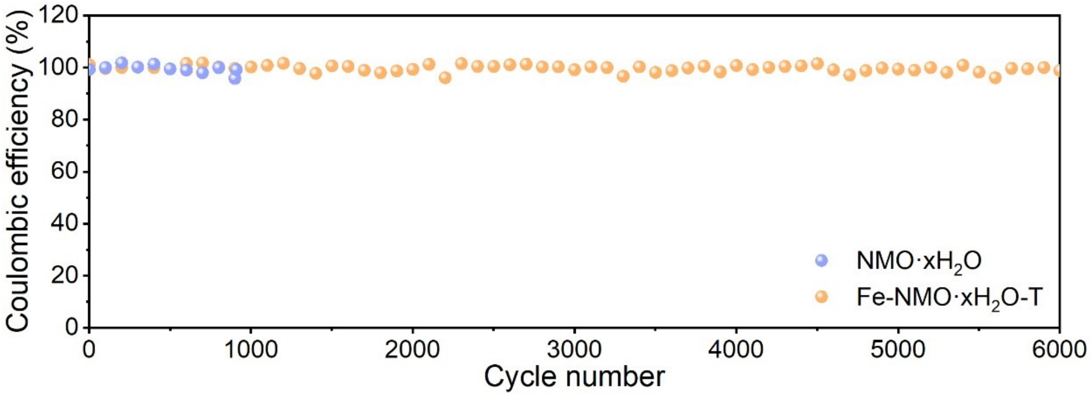

Fig. S10 Coulombic efficiencies of the NMO·xH_2O and Fe-NMO·xH_2O-T cathodes.

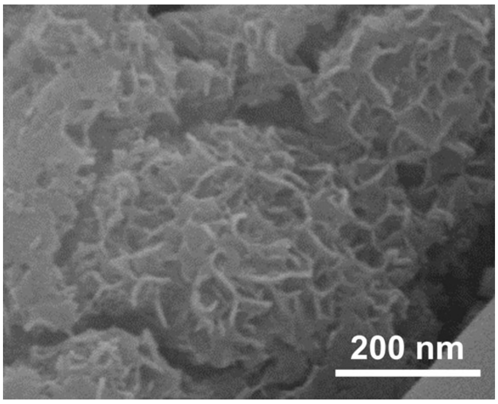

Fig. S11 FESEM image of Fe-NMO·xH_2O after the cycling test.

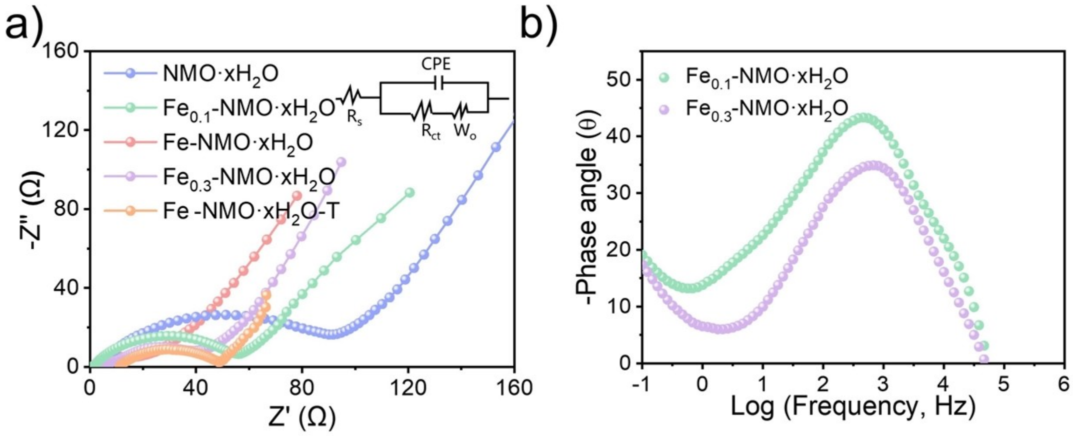

Fig. S12 (a) EIS spectra of the NMO·xH_2O, $Fe_{0.1}$-NMO·xH_2O, Fe-NMO·xH_2O, $Fe_{0.3}$-NMO·xH_2O and Fe-NMO·xH_2O-T cathodes, and (b) Bode phase angle plots of the $Fe_{0.1}$-NMO·xH_2O and $Fe_{0.3}$-NMO·xH_2O cathodes.

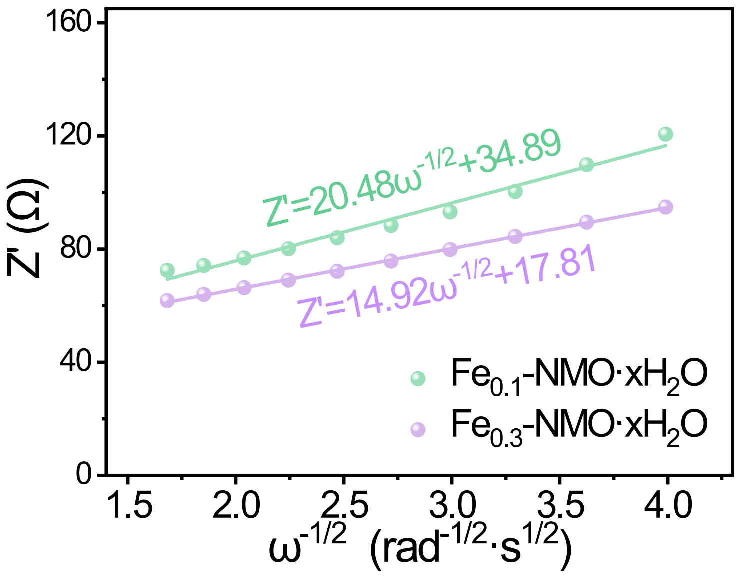

Fig. S13 The relationships between the impedance in the real part and low frequencies of the $Fe_{0.1}$-NMO·xH_2O and $Fe_{0.3}$-NMO·xH_2O cathodes.

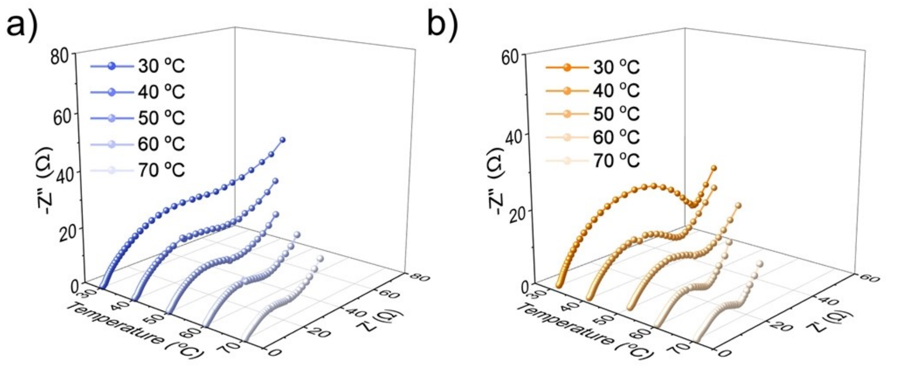

Fig. S14 EIS spectra at different temperatures of the (a) NMO·xH_2O and (b) Fe-NMO·xH_2O-T cathodes.

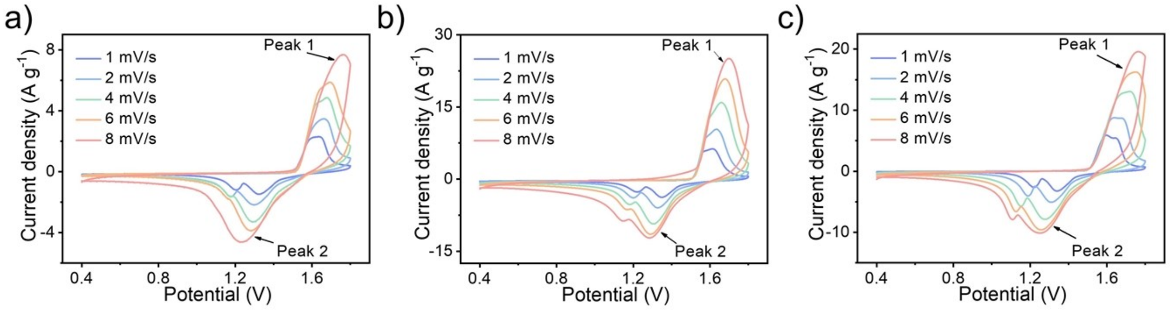

Fig. S15 CV curves of the (a) NMO·xH_2O, (b) Fe-NMO·xH_2O, and (c) Fe-NMO·xH_2O-T cathodes at various scan rates from 1 to 8 mV s^{-1}.

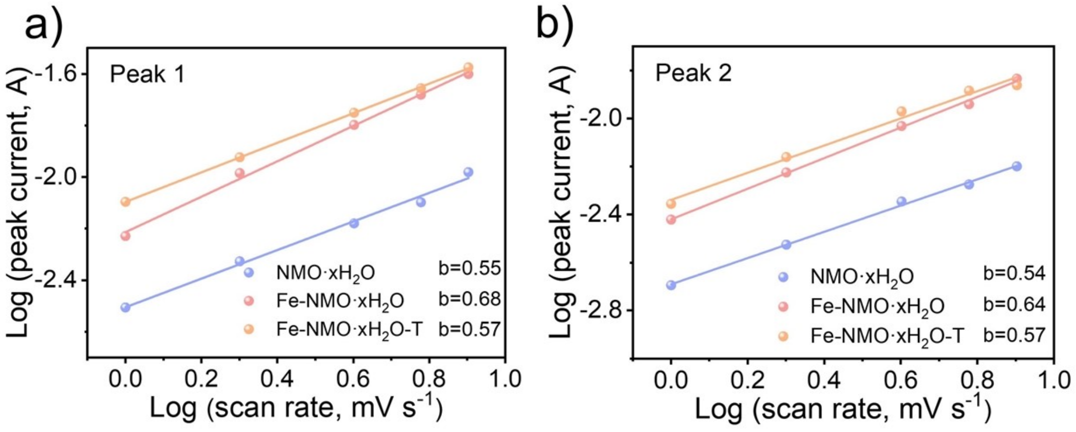

Fig. S16 Relationship between the (a) anodic peak 1 and (b) cathodic peak 2 currents and scan rates for the NMO·xH_2O, Fe-NMO·xH_2O, and Fe-NMO·xH_2O-T cathodes.

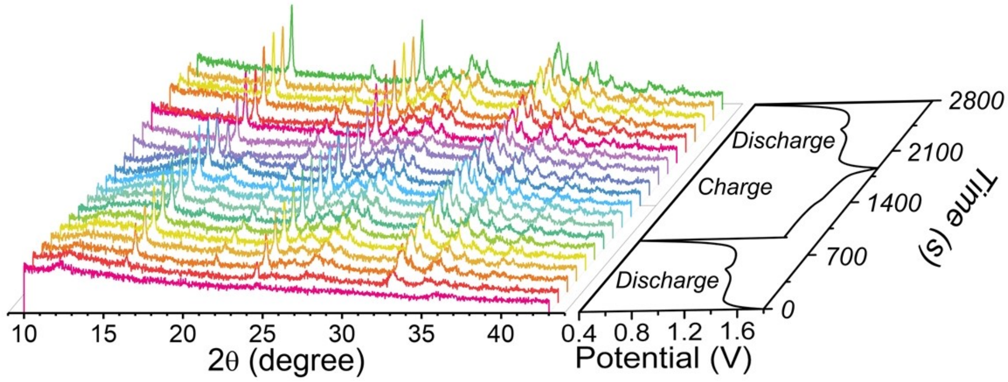

Fig. S17 In situ XRD patterns of the Fe-NMO·xH_2O during the GCD process.

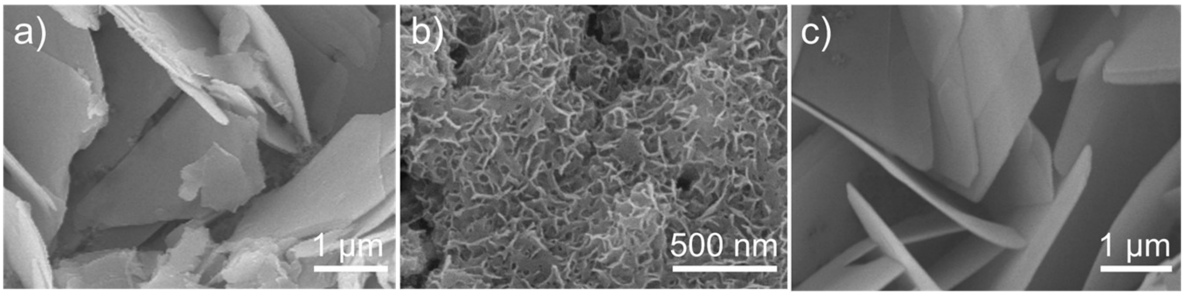

Fig. S18 Ex situ FESEM images of the Fe-NMO·xH_2O cathode at (a) fully discharged state, (b) fully charged state, and (c) re-discharged state.

Supplementary Tables

Table S1 Detailed cell parameters of the NMO·xH_2O, Fe-NMO·xH_2O, Fe-NMO·xH_2O-T and based on Rietveld refinements.

Samples	**a（Å）**	**b（Å）**	**c（Å）**	**R_{wp}**
NMO·xH_2O	5.18	2.84	7.22	7%
Fe-NMO·xH_2O	5.16	2.78	7.17	9%
Fe-NMO·xH_2O-T	5.17	2.83	6.83	6%

Table S2 Comparisons of the specific capacity of Fe-NMO·xH_2O with the previously reported electrode materials.

Cathodes	Maximum Capacity (mAh g^{-1})	Refs.
Fe-NMO·xH_2O	**307 mAh g^{-1} at 0.2 A g^{-1}**	**This work**
δ-MnO_2	219.58 mAh g^{-1} at 1.5 mA cm^{-2}	Adv. Sci. 2020, 7, 1902795.
MoS_2/PEDOT	306.6 mAh g^{-1} at 0.1 A g^{-1}	Angew. Chem. Int. Ed. 2022, 61, e202211478.
KZnHCF	68.1 mAh g^{-1} at 1 A g^{-1}	Adv. Energy Mater. 2021, 11, 2102342.
G-NCGs	113.8 mAh g^{-1} at 0.5 A g^{-1}	Adv. Funct. Mater. 2021, 31, 2100443.
PANI with PAGE	174.3 mAh g^{-1} at 0.5 A g^{-1}	Angew. Chem. Int. Ed. 2023, 135, e202215060.
PA-$VOPO_4$·2H_2O	268.2 mAh g^{-1} at 0.1 A g^{-1}	Energy Environ. Sci., 2021, 14, 4095.
$K_{1.6}Mn_{1.2}Fe(CN)_6$	65 mAh g^{-1} at 0.05 A g^{-1}	Energy Storage Mater. 2020, 29, 246.
PFC-8	139.4 mAh g^{-1} at 2.5 A g^{-1}	Angew. Chem. Int. Ed. 2022, 61, e202209794.
$Zn_{0.5}Mn_2O_4$	299.7 mAh g^{-1} at 0.1 C	Adv. Energy Mater. 2023, 13, 2203915.
PTD-1	145.56 mAh g^{-1} at 0.1 A g^{-1}	Angew. Chem. Int. Ed. 2021, 60, 20826.

Table S3 Comparisons of the rate performance of Fe-NMO·xH_2O with the state-of-the-art manganese oxide-based electrode materials.

Cathodes	**Rate Capability**	**Refs.**
Fe-NMO·xH_2O	**61% from 0.2 to 2 A g^{-1}** **33% from 0.2 to 20 A g^{-1}**	**This work**
MnO_2/MoO_3	33% from 0.2 to 2 A g^{-1}	ACS Nano 2023, 17, 15, 14792.
$Mg_{0.9}Mn_3O_7\cdot 2.7H_2O$	42% from 0.2 to 5 A g^{-1}	Adv. Energy Mater. 2022, 12, 2201840.
MnO_2/2.2 V-hold	36% from 0.2 to 2 A g^{-1}	Energy Storage Mater. 2023, 56, 524.
MnO/MZ	20% from 0.1 to 5 A g^{-1}	Adv. Funct. Mater. 2022, 32, 2106994.
Ni-Mn_2O_3	54% from 0.1 to 1 A g^{-1}	Adv. Funct. Mater. 2021, 31, 2009412.
a-$MnBO_x$	22% from 0.3 to 20 A g^{-1}	Adv. Sci. 2023, 10， 2205794.
MnS/MnO	50% from 0.1 to 2 A g^{-1}	Energy Storage Mater. 2022, 52, 180.
KMO-V	30% from 0.1 to 1 A g^{-1}	Nano Energy 2022, 98, 107274.
BMO-6	28% from 0.1 to 3 A g^{-1}	Energy Storage Mater. 2022, 48, 212.
K-MnO_x	31% from 0.1 to 2 A g^{-1}	Adv. Sci. 2023, 10, 2207329.

Table S4 Comparisons of the energy and power densities of the Zn//Fe-NMO·xH_2O device with other state-of-the-art ZIBs.

Cathodes	**Voltage window (V)**	**Maximum Energy Density (Wh kg^{-1})**	**Maximum Power Density (W kg^{-1})**	**Refs.**
Fe-NMO·xH_2O	**0.4−1.8**	**415.3**	**27638**	**This work**
$NH_4V_4O_{10}$	0.3−1.7	228	2533	Adv. Funct. Mater. 2021, 31, 2107652.
MnO	0.8−1.8	383.88	\	Energy Storage Mater. 2020, 24, 394.
N-CNSs@MnO_2	1.0−1.8	361.5	10600	Energy Storage Mater. 2020, 29 52.
$Na_4VMn(PO_4)_3$@GN	0.4−2.0	309.7	\	Adv. Energy Mater. 2022, 12, 2200654.
DTT	0.3−1.4	126.5	1760.8	Adv. Mater. 2020, 32, 2000338.
$ZnMn_2O_4$	0.6−1.9	243	6480	Energy Storage Mater. 2020, 28 407.
$KV_2O_4PO_4 \cdot 3.2H_2O$	0.2−1.8	193.8	7200	Adv. Mater. 2020, 32, 2003592.
Co-Mn_3O_4/CNA	0.2−2.2	463.1	3111.3	Adv. Energy Mater. 2021, 11, 2003203.
Poly(1,5-NAPD)	0.1−1.8	195	10000	Energy Storage Mater. 2020, 28, 64.

Table S5 Comparisons of the cycling life of Fe-NMO·xH_2O with the state-of-the-art manganese-based electrode materials.

Cathodes	**Cycling Life**	**Refs.**
Fe-NMO·xH_2O	**6,000 cycles at 5 A g^{-1}**	**This work**
$Na_4VMn(PO_4)_3$@GN	3,000 cycles at 5 A g^{-1}	Adv. Energy Mater. 2022, 12, 2200654.
MMO-2	1,000 cycles at 5 A g^{-1}	Adv. Funct. Mater. 2023, 33, 2301351.
MnVO@C	4,000 cycles at 5 A g^{-1}	Energy Environ. Sci., 2021, 14, 3954.
$(Na_{0.33}, Mn_{0.65})V_8O_{20}\cdot nH_2O$	1,000 cycles at 4 A g^{-1}	Adv. Sci. 2020, 7, 2000083.
Ce-MnO_2	2,000 cycles at 6 C	Adv. Funct. Mater. 2023, 33, 2303009.
MG	3,000 cycles at 6 C	Energy Storage Mater. 2022, 52, 675.
Cu-MnO_2	1,000 cycles at 3 A g^{-1}	Angew. Chem. Int. Ed. 2023, 62, e202215654.
MnO_2@PDAAQ	2,200 cycles at 3 A g^{-1}	Energy Storage Mater. 2022, 52, 675.
$ZnMn_2O_4$@C	2,000 cycles at 3 A g^{-1}	Adv. Sci. 2021, 8, 2002636.

Table S6 Simulation parameters of the EIS spectra for NMO·xH_2O, $Fe_{0.1}$-NMO·xH_2O, Fe-NMO·xH_2O, $Fe_{0.3}$-NMO·xH_2O, and Fe-NMO·xH_2O-T.

Samples	**R_s (Ω)**	**R_{ct} (Ω)**	**W_o (Ω)**
NMO·xH_2O	6.34	101.20	18.63
$Fe_{0.1}$-NMO·xH_2O	1.13	58.70	14.86
Fe-NMO·xH_2O	0.86	20.82	3.03
$Fe_{0.3}$-NMO·xH_2O	4.46	42.70	4.60
Fe-NMO·xH_2O-T	8.05	48.02	6.11

Table S7 Simulation parameters of the in situ EIS spectra for Fe-NMO·xH_2O.

	Potential (V)	**R_s (Ω)**	**R_{ct} (Ω)**	**W_o (Ω)**
Discharge Process	1.8	1.02	21.21	1.26
	1.4	1.85	49.65	2.37
	1.0	2.98	80.02	6.12
	0.7	3.87	141.31	9.13
	0.4	6.95	196.44	13.30
Charge Process	0.4	6.95	196.44	13.30
	0.7	5.29	111.70	8.54
	1.0	3.76	76.88	4.80
	1.4	2.04	53.48	2.96
	1.8	1.23	25.70	1.52

Supplementary References

[1] P. Hohenberg and W. Kohn, *Phys. Rev.*, 1964 , **136**, B864-B871.

[2] W. Kohn and L. J. Sham, *Phys. Rev.*, 1965, **140**, A1133-A1138.

[3] P. E. Blöchl, *Phys. Rev. B*, 1994, **50**, 17953-17979.

[4] G. Kresse and J. Hafner, *Phys. Rev. B*, 1993, **47**, 558-561.

[5] J. P. Perdew, K. Burke and M. Ernzerhof, *Phys. Rev. lett.*, 1996, **77**, 3865-3868.

[6] C. Chen, K. Xu, X. Ji, B. Zhang, L. Miao and J. Jiang, *J. Mater. Chem. A*, 2015, **3**, 12461-12467.

[7] S. Grimme, S. Ehrlich and L. Goerigk, *J. Comput. Chem.*, 2011, **32**, 1456-1465.

[8] V. Wang, N. Xu and J. C. Liu, et al., *Comput. Phys. Commun.*, 2021, **267**, 108033.

[9] K. Momma and F. Izumi, *J. Appl. Crystallogr.*, 2011, **44**, 1272-1276.